



High-precision star-formation efficiency measurements in nearby clouds

Zipeng Hu , ¹★ Mark R. Krumholz , ^{1,2} Riway Pokhrel ³ and Robert A. Gutermuth ⁴

¹Research School of Astronomy and Astrophysics, Australian National University, Canberra, ACT 2611, Australia

²ARC Centre of Excellence for Astronomy in Three Dimensions (ASTRO-3D), Canberra, ACT 2611, Australia

³Ritter Astrophysical Research Center, Department of Physics and Astronomy, University of Toledo, Toledo, OH 43606, USA

⁴Department of Astronomy, University of Massachusetts, 710 North Pleasant Street, Amherst, MA 01003, USA

Accepted 2022 January 19. Received 2022 January 16; in original form 2021 September 10

ABSTRACT

On average molecular clouds convert only a small fraction ϵ_{ff} of their mass into stars per free-fall time, but different star-formation theories make contrasting claims for how this low mean efficiency is achieved. To test these theories, we need precise measurements of both the mean value and the scatter of ϵ_{ff} , but high-precision measurements have been difficult because they require determining cloud-volume densities, from which we can calculate free-fall times. Until recently, most density estimates treated clouds as uniform spheres, while their real structures are often filamentary and highly non-uniform, yielding systematic errors in ϵ_{ff} estimates and smearing real cloud-to-cloud variations. We recently developed a theoretical model to reduce this error by using column-density distributions in clouds to produce more accurate volume-density estimates. In this work, we apply this model to recent observations of 12 nearby molecular clouds. Compared to earlier analyses, our method reduces the typical dispersion of ϵ_{ff} within individual clouds from 0.16 to 0.12 dex, and decreases the median value of ϵ_{ff} over all clouds from ≈ 0.02 to ≈ 0.01 . However, we find no significant change in the ≈ 0.2 dex cloud-to-cloud dispersion of ϵ_{ff} , suggesting the measured dispersions reflect real structural differences between clouds.

Key words: ISM: structure – stars: formation.

1 INTRODUCTION

Star formation is inefficient. A star-forming region with little resistance to self-gravity will convert its gaseous mass to stars within a single free-fall time $t_{\text{ff}} = \sqrt{3\pi/32G\rho}$, where ρ is the volume density. The ratio of the actual gas-depletion time t_{dep} to t_{ff} is called the star-formation efficiency per free-fall time ϵ_{ff} (Krumholz & McKee 2005). Zuckerman & Evans (1974) were the first to point out that the observed star-formation rate of the Milky Way as a whole implies that, averaged over all molecular clouds, $\epsilon_{\text{ff}} \ll 1$. Krumholz & Tan (2007) extended this conclusion to the denser parts of molecular clouds traced by hydrogen cyanide (HCN), and more recent work has obtained $\epsilon_{\text{ff}} \sim 0.01$ both for nearby clouds (e.g. Evans, Heiderman & Vutisalchavakul 2014; Heyer et al. 2016; Lee, Miville-Deschênes & Murray 2016; Ochsendorf et al. 2017) and for ~ 100 pc-scale patches in nearby galactic discs (e.g. Krumholz, Dekel & McKee 2012; Utomo et al. 2018). The study-to-study dispersion in ϵ_{ff} is ≈ 0.3 dex, while the dispersion within any single study is about 0.3–0.5 dex (Krumholz, McKee & Bland-Hawthorn 2019).

Theoretical efforts to explain the origin of observed low ϵ_{ff} values can be categorized into two main types. Some theories focus on galactic scale physical processes (e.g. Kim, Kim & Ostriker 2011; Ostriker & Shetty 2011; Faucher-Giguère, Quataert & Hopkins 2013), while others are developed from internal star-formation regulation processes within individual molecular clouds (e.g. Elmegreen & Parravano 1994; Krumholz & McKee 2005; Hennebelle & Chabrier 2011; Krumholz, Leroy & McKee 2011a;

Federrath & Klessen 2012; Padoan, Haugbølle & Nordlund 2012). Despite predicting similarly low mean ϵ_{ff} values, the two types of models yield significantly different estimates for the dispersion of ϵ_{ff} – models regulated on the cloud scale generally predict much smaller dispersions than those regulated on the galactic scale (Lee et al. 2016; Krumholz & McKee 2020). Therefore, it is important to measure cloud-scale ϵ_{ff} values with enough fidelity to extract both its mean value and dispersion. The most accurate measurements to date are those of Pokhrel et al. (2021), thanks to two advantages over previous studies: First, they derived their column-density maps from *Herschel* dust-emission maps, which allow them to sample a substantially larger dynamic range of column density than previous studies using extinction maps. Second, they use the SESNA catalogue (Gutermuth et al., in preparation) of young stellar objects (YSOs), which is much more complete in dense regions than earlier catalogues, and for the first time includes accurate corrections for contamination by extragalactic interlopers and edge-on discs (Gutermuth et al. 2008, 2009). They determine a median value $\log \epsilon_{\text{ff}} = -1.59$ with a dispersion of 0.18 dex in a sample of 12 nearby molecular clouds.

However, most previous ϵ_{ff} measurements, including those of Pokhrel et al. (2021), incur a substantial error when calculating the volume density, which is required for the free-fall time. The fundamental challenge is that the volume density is a 3D quantity, which is not directly accessible in a 2D observation. The most common practice in literature is to estimate the density by assuming that the area of interest is the projection of a uniform sphere, whose radius is equal to the mean radius of the projected shape. For a cloud with a total projected area A and a total mass M , this approximation gives a density estimate $\rho_{\text{sph}} = 3M/4\sqrt{A^3/\pi}$. This method has been used by a number of studies in the Milky Way (e.g. Krumholz,

* E-mail: zphu.charles@gmail.com

Dekel & McKee 2011b; Lada et al. 2013; Evans et al. 2014; Pokhrel et al. 2021) and in the Large Magellanic Cloud (Ochsendorf et al. 2017). While simple, this procedure likely introduces significant systematic errors, coming from two primary sources. One is that in the past decades, it has become clear that the interstellar medium is characterized mainly by filamentary structures (e.g. Schneider & Elmegreen 1979; Dobashi et al. 2005; Arzoumanian et al. 2011; André et al. 2014; Kainulainen et al. 2016), which results in elongated contours identified from column-density maps. The mean density of such structure is likely to be different from that calculated with spherical assumption. Second, for fixed ϵ_{ff} , the star-formation rate in a given volume of gas will be $\epsilon_{\text{ff}} \int (\rho/t_{\text{ff}}) dV$, and thus the quantity of interest for measuring ϵ_{ff} is the mass-weighted mean of t_{ff}^{-1} . Since the relationship between free-fall time and density is non-linear, $t_{\text{ff}} \propto \rho^{-1/2}$, this is not identical to the free-fall time computed from the mean volume density, which is what the spherical assumption measures. In a medium containing significant density structure, the two can differ substantially (e.g. Hennebelle & Chabrier 2011; Federrath & Klessen 2012; Federrath 2013; Salim, Federrath & Kewley 2015).

Hu et al. (2021, hereafter H21) recently proposed an alternative approach to estimate the free-fall time-weighted mean density ρ_{eff} , which is defined as

$$\rho_{\text{eff}} = \left(\frac{\int \rho^{3/2} dV}{\int \rho dV} \right)^2, \quad (1)$$

where ρ is the local volume density and the integral is over the cloud volume. This method immediately yields the correct free-fall time for the purposes of estimating ϵ_{ff} . H21 analyse star-formation simulations from Cunningham et al. (2018), and show that one can estimate ρ_{eff} with higher accuracy than is obtained from the simple spherical assumption by making use of the full 2D column-density distribution, rather than simply its mean. Applied to simulations, their method corrects a ≈ 0.13 dex overestimation and removes a ~ 0.25 dex scatter in ϵ_{ff} caused by spherical assumption. In this paper, we apply this model to the observations of Pokhrel et al. (2020, 2021) in order to derive higher accuracy ϵ_{ff} measurements than have previously been possible. We summarize the observations in Section 2, introduce the Hu et al. model in Section 3.1, describe its application to the data in Section 3.2, present the results of the analysis in Section 4, and draw conclusions in Section 5.

2 OBSERVATIONS

Our data-reduction and analysis method is described in Pokhrel et al. (2020), and full details are provided there. Here, we simply summarize for convenience. This study analyses 12 nearby star-forming regions: Ophiuchus, Perseus, Orion-A, Orion-B, Aquila-North, Aquila-South, NGC 2264, S140, AFGL 490, Cep OB3, Mon R2, and Cygnus-X. For each region we have a matched protostellar catalogue and cloud column-density map. The latter are derived from *Herschel*/PACS and *Herschel*/SPIRE imaging at 160, 250, 350, and 500 μm , convolved to a common resolution (André et al. 2010). To obtain the column density in each pixel, we fit the spectral-energy distribution with a dust-emission model where the only two free parameters are the temperature and the column density. The best-fitting column density can be equivalently expressed in column of H_2 molecules, $N(\text{H}_2)$, or column of gas mass Σ_{gas} , which are related by $\Sigma_{\text{gas}} = 2m_{\text{H}}/X N(\text{H}_2)$, where $m_{\text{H}} = 1.67 \times 10^{-24}$ g is the hydrogen atom mass and $X = 0.71$ is the hydrogen mass fraction of the local interstellar medium (Nieva & Przybilla 2012). On the obtained column-density map, we first mask pixels with the best-fitting dust temperature, which implies that the dust in that pixel falls

on the Rayleigh–Jeans tail of the modified blackbody spectrum across all *Herschel* bands, since in this case our fits represent only lower limits on the temperature, and thus the best-fitting column densities are only upper limits. The exact temperature limits are provided in table 2 of Pokhrel et al. (2020). Second, we mask pixels with derived column densities $N(\text{H}_2) > 10^{23} \text{ cm}^{-2}$, because for these dust optical depth effects can be significant and thus fitted $N(\text{H}_2)$ values may only represent lower limits. The effect of both masks is negligible in our results, since for all clouds the masked regions constitute less than 0.5 per cent of the cloud by either area or mass, and, for many clouds, no pixels are masked at all.

The SESNA catalogue (Gutermuth et al., in preparation) we use for protostars is a combination of *Spitzer* and Two Micron All-Sky Survey observations (Skrutskie et al. 2006), spanning about 90 deg^2 . For the farthest target Cygnus-X, the deeper UKIDSS (Lawrence et al. 2007) near-infrared (IR) Galactic Plane Survey (Lucas et al. 2008) is used. We mask parts of column-density maps outside SESNA coverage. After removing field stars, we classify sources in the SENA field with excess IR emission as Class I YSOs (embedded protostars), Class II YSOs (which have cleared their envelopes, but retain circumstellar discs), or contaminants by using flux selections and a series of reddening-safe colours (Gutermuth et al. 2009). We calculate ϵ_{ff} from the counts of Class I YSOs, since these have a short lifetime of ≈ 0.5 Myr, and thus are less sensitive to time-varying star-formation rates than Class II objects, which integrate over ≈ 2 Myr (see discussion in section 5.1 of Pokhrel et al. 2020).

Before analysing the data, we must first remove two types of contaminants. First, Class II objects may be misclassified as Class I if they are edge-on and the disc occults the central star. The median misclassification rate from recent studies (Gutermuth et al. 2009; Kryukova et al. 2012, 2014) is 3.5 per cent, and we therefore reduce the count of Class I objects by 3.5 per cent of the total count of Class II objects in the same area. Second, there are 4.5 ± 0.5 extragalactic contaminants per square degree whose colours are similar enough to YSOs for them to be included in the SENA catalogue for Class I objects. To compensate, we subtract 4.5 objects per square degree from our Class I YSO counts.

A final correction applies only to Cygnus-X, our most distant target. The YSO sensitivity for the SESNA catalogue is $\sim 0.1 M_{\odot}$ for all other clouds, but in the case of Cygnus-X, its relatively large distance ($\sim 1400 \text{ pc}$), denser field stars, more regions of bright nebosity, and shallower infrared array camera (IRAC) data result in a much lower YSO sensitivity ($\sim 1 M_{\odot}$). Assuming a Chabrier (2003) initial mass function, this implies that the fraction of detected YSOs is 0.163 of the total present. Thus, we divide the Class I object count in Cygnus-X by this fraction to achieve a uniform sensitivity of $0.1 M_{\odot}$ in our sample.

3 METHODS

To predict the free-fall time-weighted mean density ρ_{eff} from the spherical density ρ_{sph} , we apply the method of H21 to contours generated from the *Herschel* column-density maps. We first briefly introduce the model in Section 3.1, and then we present the application of this model to the observations in Section 3.2.

3.1 H21 model

To determine the relationship between ρ_{eff} and ρ_{sph} , H21 analysed simulations of the formation of low-mass star clusters in a dense molecular clump by Cunningham et al. (2018). These simulations include gravity, magnetic fields, turbulence, radiation feedback, and

protostellar jets/outflows. Adopting a periodic box size of 0.65 pc, a dynamic resolution range of (1.6×10^{-4} pc, 2.5×10^{-3} pc), and gas with solar metallicity, they produce star-formation efficiencies consistent with observations. We refer readers to Cunningham et al. (2018) for full details.

H21 construct synthetic dust observations of the simulations, and draw column-density contours on the projected images at a range of column densities. For each contour that encloses one or more protostars, they measure both the true effective density ρ_{eff} of the enclosed mass and the density ρ_{sph} that one would derive from the spherical assumption. They also consider a number of other projected quantities that would be accessible to an observer, in order to search for an estimator for ρ_{eff} more accurate than just ρ_{sph} . They find that using the Gini coefficient g of the column densities enclosed by a contour allows a substantially better prediction of ρ_{eff} , and define the new estimator

$$\rho_g = 10^{k_g - b} \rho_{\text{sph}}, \quad (2)$$

where ρ_g is the predicted value of ρ_{eff} , and $k = 4.6$ and $b = 0.93$ are coefficients determined by fitting the simulated data. We discuss how these are modified in the presence of observational bias in Section 3.2.

In order to accomplish our goal of obtaining high-accuracy estimates of ϵ_{ff} , it is important to understand the uncertainties in this relation. Although the values of k and b are fitted from exact simulation data without error bars, we can none the less estimate the errors on these quantities from bootstrapping. We randomly choose elements from simulation sample with replacement until we obtain a new sample with the same size as before. Then we fit equation (2) on this new sample and repeat this process for 10^4 times. We take our uncertainties to be the 16th and 84th percentiles of the fitted k and b values, which give $k = 4.6 \pm 0.1$ and $b = 0.93 \pm 0.03$. These errors are small enough that they are unimportant compared to the other effects we discuss below.

The mean of residual between ρ_g and ρ_{eff} is 0.18 dex. While this is a substantial improvement over ρ_{sph} (for which the residual is 0.42 dex), the mean residual of our model should still be considered as an error source in the calculation of ϵ_{ff} of a single region. When determining the overall mean ϵ_{ff} and its dispersion, however, we are calculating mean values and percentiles from a sample of many contours. In the analysis we present below, each measurement we make will represent an average over at least 20 distinct contours, with implies an upper limit of 0.04 dex on the contribution of our imperfect estimate of ρ_{eff} to the overall error budget of star-formation efficiencies.

We conclude our discussion by addressing two possible concerns regarding the **H21** method. First, the method implicitly assumes that star-forming clouds are approximately self-similar, so that the relationship between ρ_{eff} and ρ_{sph} is not determined by tiny-scale density structures that do not have any counterpart in the column-density structure measured on scales accessible to the observations. This is an assumption, but it is a plausible one given both the simulations and the available observations. On the simulation side, **H21** show that the absolute sizes of contours are very poor predictors of the $\rho_{\text{eff}} - \rho_{\text{sph}}$ relationship – exactly what we expect if the structure is close to self-similar. With respect to observations, we note that, due to the different distances of the clouds in our sample, the *Herschel* column-density maps cover a resolution range from 0.02 to 0.24 pc. We do not find systematic differences in cloud structure between clouds observed with lower or higher physical resolution, indicating the self-similar assumption is valid at least within this range of scales.

A second concern is that, while **H21** show that estimates of ϵ_{ff} derived from ρ_g , which we denote $\epsilon_{\text{ff},g}$ are unbiased in the sense that

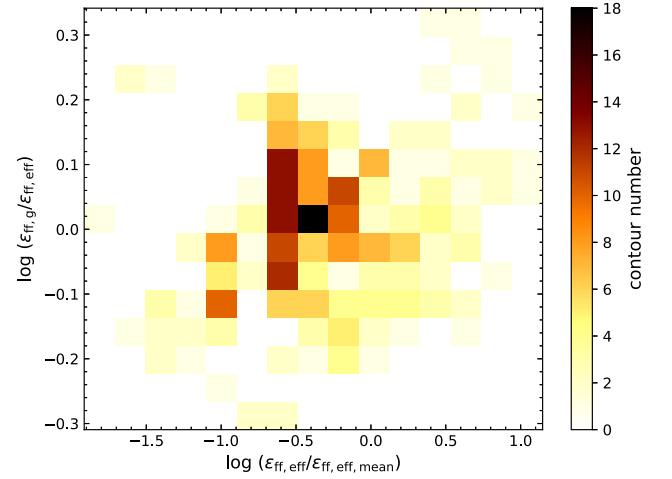


Figure 1. 2D distribution plot of $(\epsilon_{\text{ff},g}/\epsilon_{\text{ff},\text{eff}})$ versus $(\epsilon_{\text{ff},\text{eff}}/\epsilon_{\text{ff},\text{eff},\text{mean}})$. The values are determined from simulation contours, and the colour shows the number of contours in each bin.

the expectation value of $\epsilon_{\text{ff},g}$ matches the true value of ϵ_{ff} , this does not automatically guarantee that estimates for the *dispersion* of ϵ_{ff} values derived using ρ_g , which we denote σ_g , represent an unbiased estimate of the intrinsic dispersion σ_{eff} . Indeed, if the residual errors of the estimated $\epsilon_{\text{ff},g}$ are random, then σ_g will naturally be larger than the intrinsic dispersion σ_{eff} , which is why the goal of the **H21** model is to make the errors in $\epsilon_{\text{ff},g}$ as small as possible. However, it is in principle possible for the expectation value of σ_g to be *smaller* than σ_{eff} , if the errors in $\epsilon_{\text{ff},g}$ are correlated and directional, meaning that contours for which the true value of $\epsilon_{\text{ff},\text{eff}}$ is smaller than the mean over all contours tend to have positive errors, while for contours where the true value of $\epsilon_{\text{ff},\text{eff}}$ is larger than the mean, the errors tend to be negative. If such a correlation existed, it would artificially reduce the dispersion, leading us to underestimate rather than overestimate σ_g .

To investigate this scenario, we measure ρ_{eff} and ρ_g for each of the contours used in **H21**, and from these compute $(\epsilon_{\text{ff},g}/\epsilon_{\text{ff},\text{eff}})$ and $(\epsilon_{\text{ff},\text{eff}}/\epsilon_{\text{ff},\text{eff},\text{mean}})$, where $\epsilon_{\text{ff},\text{eff}}$ is the true star-formation efficiency (determined from the true mean effective density ρ_{eff} in the simulation), $\epsilon_{\text{ff},g}$ is the star-formation efficiency inferred using ρ_g , and $\epsilon_{\text{ff},\text{eff},\text{mean}}$ is the mean value of ϵ_{ff} over all simulation contours. We plot the joint distribution of these two ratios in Fig. 1, and it is clear that there is no significant negative correlation, as would be required to render σ_g an underestimate of σ_{eff} . Linear regression between these two ratio values returns a coefficient of determination $R^2 = 0.05$, confirming this visual impression. Thus, we expect that errors in $\epsilon_{\text{ff},g}$ are randomly directed, making the estimated star-formation efficiency dispersion σ_g an upper limit of the intrinsic dispersion σ_{eff} .

3.2 Application to *Herschel* observations

The first step in applying our method to the *Herschel* observations is to generate column-density contours across the full range of $N(\text{H}_2)$ covered by the observations. For each of the 12 regions, we start by finding the lowest $N(\text{H}_2)$ value such that all pixels with column density above it are inside the SESNA coverage; equivalently, we set the minimum value of $N(\text{H}_2)$ to be the lowest possible choice such that the contour sits entirely within the SENSAs footprint. We define M_0 as the total gas mass enclosed by this contour. We then draw 100 $N(\text{H}_2)$ contours at higher $N(\text{H}_2)$, with the levels chosen such that the total mass above each level is equally spaced from M_0 to $M_0/100$ with

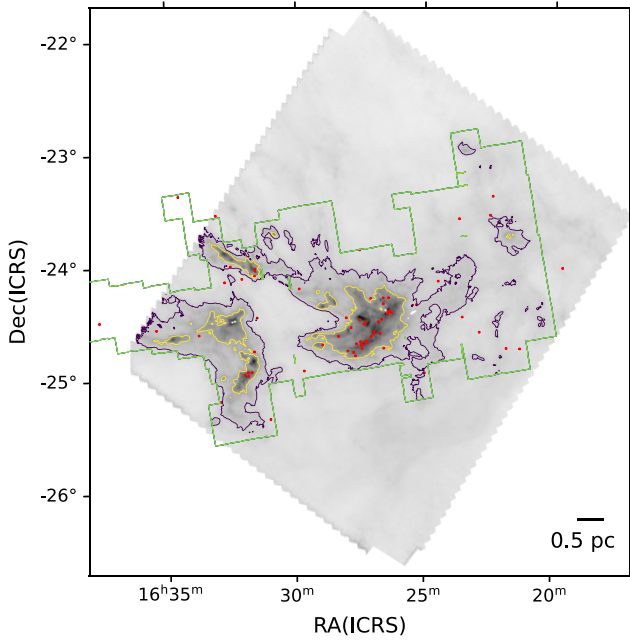


Figure 2. A column-density map of the Ophiuchus cloud derived from *Herschel* observations. The green contour is the Spitzer coverage area, and we illustrate the largest contour that fits within this footprint in purple; the yellow contour is set at a level that encloses half as much mass as the purple one. The red dots are the positions of protostars.

a step of $M_0/100$; we only retain contours that contain at least one protostar, consistent with the selection we apply to the simulations in H21. We show an example of Ophiuchus cloud column-density map with $N(\text{H}_2)$ contours, protostar positions, and SESNA coverage area in Fig. 2.

For every contour, we measure four values: total gas mass M_{gas} , total area A , completeness-corrected total protostar number N_{PS} , and the Gini coefficient g of the surface density of all pixels within the contour (see H21 for details). From these parameters, we derive five additional quantities: mean gas surface density $\Sigma_{\text{gas}} = M_{\text{gas}}/A$, star-formation surface density Σ_{SFR} , the volume density ρ_{sph} , and free-fall time derived from the spherical assumption $t_{\text{ff,sph}}$ (see Section 1), and the corresponding star-formation efficiency per free-fall time $\epsilon_{\text{ff,sph}}$. To calculate Σ_{SFR} , we assume the mean mass of protostars in SESNA to be $M_{\text{PS}} \approx 0.5 M_{\odot}$ (Evans et al. 2009), and the mean duration of protostellar phase included in SESNA observations to be $t_{\text{PS}} \approx 0.5$ Myr (Dunham et al. 2014, 2015). Thus, $\Sigma_{\text{SFR}} = N_{\text{PS}} M_{\text{PS}} / A t_{\text{PS}}$, and $\epsilon_{\text{ff,sph}} = \Sigma_{\text{SFR}} / (\Sigma_{\text{gas}} / t_{\text{ff,sph}})$.

Our next step is to account for the limited resolution and dynamic range of the observations, which is much smaller than that of the simulations. First, consider the effects of resolution: the *Herschel* beam will smear out the density structure on scales comparable to the beam full width at half-maximum (FWHM), and this will suppress the Gini coefficient. We must, therefore, remove from our sample contours small enough that beam smearing precludes an accurate estimate of g . To do so, for each contour we compute the ratio of the mean contour radius $r = \sqrt{A/\pi}$ to the resolution R of the *Herschel* maps (expressed as the effective beam FWHM, taken from table 1 of Pokhrel et al. 2020). To check when beam smearing becomes significant, we artificially blur our data: For each cloud, we construct eight column-density maps smeared by Gaussian beams with sizes uniformly spaced between R and $20R$, and place contours on these smeared maps exactly as we do for the original maps. We plot the

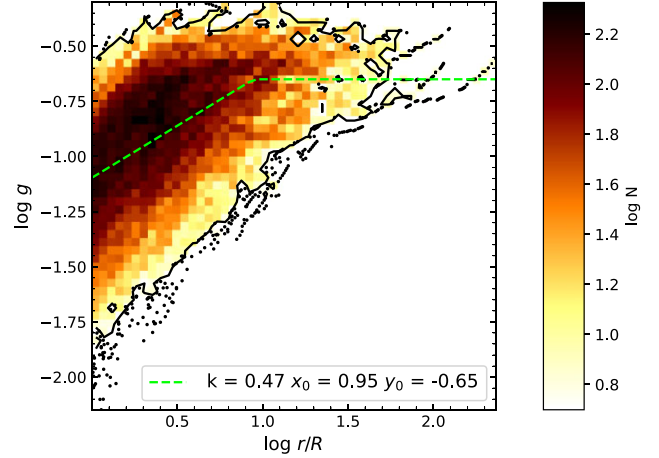


Figure 3. 2D distribution plot of g versus $\log(r/R)$. The values are determined from the smeared contours, and the colour shows the number of contours in each bin (one black dot represents one single contour). The green dash line shows the piece-wise function equation (3) fitted to this distribution.

distribution of g values for all contours with $\Sigma_{\text{SFR}} > 0$ in Fig. 3. The figure clearly shows the expected effect: Contours with small r/R have systematically smaller values of g than larger ones. To quantify this, we fit the distribution of $[\log(r/R), g]$ values with a piecewise linear function

$$g = \begin{cases} k(\log(r/R) - x_0) + y_0 & \text{if } \log(r/R) < x_0 \\ y_0 & \text{if } \log(r/R) \geq x_0 \end{cases} \quad (3)$$

where, k , x_0 , and y_0 are free parameters. The green line shows the best-fitting, $k = 0.47$, $x_0 = 0.95$, and $y_0 = -0.65$, which illustrates the effect in which we are interested: The distribution of g values becomes independent of resolution when $\log(r/R) \geq 0.95$, and drops below this threshold. Therefore, before analyzing the contours from the original, unsmeared maps, we remove all those contours with $\log(r/R) < 0.95$. We also select contours that contain at least one protostar, since we obviously cannot compute ϵ_{ff} values for those that contain none.

We perform a similar analysis to control for the effects of the limited dynamic range of the observations, i.e. the fact that there are minimum and maximum measurable values of Σ_{gas} , and this in turn imposes limits on the maximum possible value of g . Define $\eta = \Sigma_{\text{gas,min}} / \Sigma_{\text{gas,max}} < 1$ as the ratio of minimum and maximum column densities within a given map contour. The value of η necessarily limits the range of g , since as $\eta \rightarrow 1$, the column densities within the contour all become the same, and clearly we must therefore have $g \rightarrow 0$.

This effect means that we must truncate our sample by discarding contours for which $\eta > \eta_{\text{max}}$, where the value of η_{max} must be determined. To do so, we need to estimate the quantitative relation between g and η from the molecular cloud column-density distribution. Previous observations have shown that the column-density distribution of molecular clouds can be characterized by a lognormal peak and a power-law tail towards to higher end (e.g. Goodman, Pineda & Schnee 2009; Kainulainen et al. 2009; Froebrich & Rowles 2010; Lombardi, Alves & Lada 2010; Schneider et al. 2011, 2015; Pokhrel et al. 2016); we concentrate on the power-law tail, since we only select star-forming contours with column density above average, and we find that our contours do indeed have approximately power-law distributions of pixel column density, with slopes ≈ -2 . For such a distribution, $dN_p/d\Sigma_{\text{gas}} \propto \Sigma_{\text{gas}}^{-2}$, if the range of measurable column

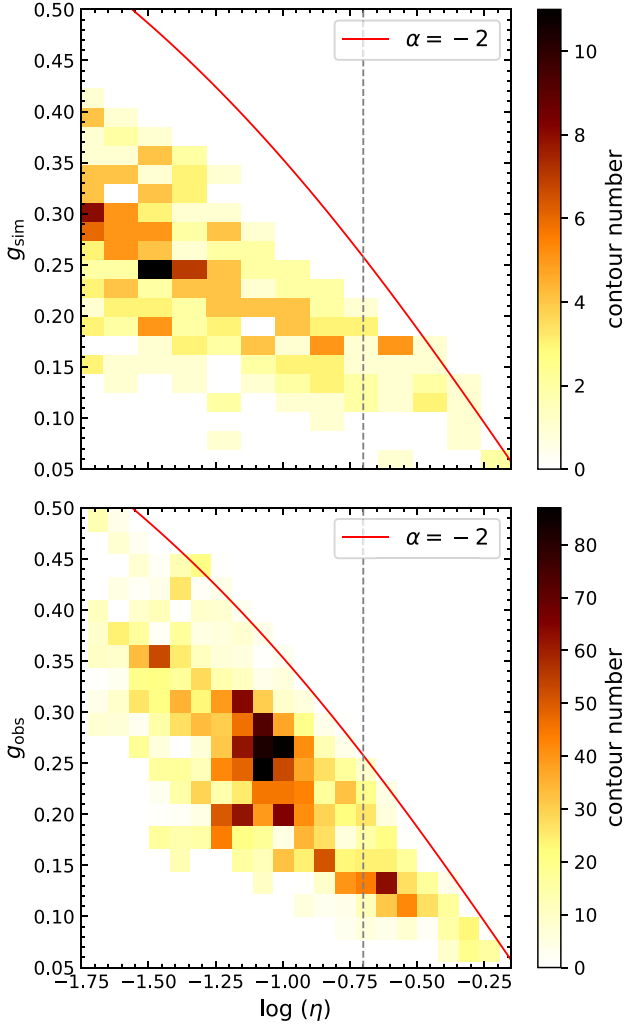


Figure 4. 2D histograms of contour Gini coefficients g and column-density range $\log(\eta)$. Top panel: Simulation contours. Bottom panel: *Herschel* map contours. The solid line plots in both panels show the theoretical value of g for contours with perfect power-law column-density distributions with $\alpha = -2$ (equation 4), the approximate value we measure in both simulations and observations; results for other values of α within the uncertainty of the fits are nearly indistinguishable. The grey dashed vertical line shows $\log(\eta) = -0.7$. Note that the simulations, which have greater dynamic range than the observations, extend well beyond the range of η shown in the plot.

densities is limited to Σ_{\min} to Σ_{\max} , the resulting Gini coefficient is

$$g = 1 - 2 \begin{cases} \frac{(3+2\alpha)\eta^{2-\alpha} - (\alpha+2)\eta^3 - (\alpha+1)\eta^{-2\alpha}}{(2\alpha+3)(\eta - \eta^{-\alpha})(\eta^{-\alpha} - \eta^2)}, & \alpha < -1, \alpha \neq -2 \\ \frac{\eta}{\eta-1} - \frac{1}{\log(\eta)}, & \alpha = -2 \end{cases}. \quad (4)$$

We can use this result to study where limited dynamic range begins to affect our results by examining the locations of our contours in the (η, g) plane – contours that lie near the upper limit suggest that our measured values of g may be compromised by limited dynamic range, while those that lie well below the limit are likely to suffer only minimal effects.

We plot 2D histograms of g versus $\log \eta$ for both our *Herschel* observations and for the C18 simulations, together with equation (4), in Fig. 4. We see that, for both the simulations and observations, the distribution approaches the limit as $\eta \rightarrow 1$, but falls significantly below it when $\eta \ll 1$. Based on this figure, we choose to truncate our sample at $\log \eta_{\max} = -0.7$, since for both the simulations and

the observations the data approach the maximum value of g for $\log \eta > -0.7$, but fall well below it for smaller η .

To ensure that our truncation of the sample at both small radii and small dynamic range does not create an inconsistency between the observations and our simulations, we apply the same cuts to the simulations and refit the relationship between ρ_{eff} , ρ_{sph} , and g , using the same method as described in H21. Doing so yields $k = 4.3 \pm 0.1$, $b = 0.84 \pm 0.04$, and a coefficient of determination $R^2 = 0.70$. The error range of k and b are obtained from half-sample fitting as described in Section 3.1. Such values are close to previous ones. For consistency, we will use the new fitted model coefficients throughout the rest of this manuscript.

Applying the down-selections described above to the *Herschel* data, we obtain 2905 contours that form the data set for further analysis. For all selected contours, we apply equation (2) (with the modified values of k and b) to determine their effective volume density ρ_g , and replace ρ_{sph} with ρ_g to recalculate the new result star-formation efficiency denoted as $\epsilon_{\text{ff},g}$.

4 RESULTS

With the properties determined from the unsmeared contours on different surface-density levels, we first investigate how the triplet $(g, \epsilon_{\text{ff},\text{sph}}, \epsilon_{\text{ff},g})$ changes with Σ_{gas} . In Fig. 5, we show the 2D histogram of g versus $\log(\Sigma_{\text{gas}})$. We can find no significant relation between g and Σ_{gas} in this plot, which is consistent with the simulation results. The median value of g is $g_{\text{median}} = 0.24$, which is above 0.2, the value for a uniform-density sphere (H21). This indicates that the free-fall time of most contours will be overestimated by the spherical assumption. For a typical Gini coefficient $g = 0.24$, our estimated uncertainties on k and b in equation (2) translate to an increase in the dispersion of ϵ_{ff} by 0.01 dex, which is negligible. For this reason, we will simply treat k and b as constants fixed to their central values for the remainder of this analysis. Similarly, given that we have an average of 300 contours per cloud, the 0.18 dex mean residual scatter of the H21 model corresponds to only a ~ 0.005 dex scatter in the percentiles and mean values of ϵ_{ff} , negligibly small.

To study the difference between estimates of ϵ_{ff} derived using the spherical assumption and our improved method, we define two quantities: the mean star-formation efficiency for an individual cloud ($\langle \epsilon_{\text{ff}} \rangle$), and the mean dispersion in star-formation efficiency σ . We compute these as follows: For each cloud, we sort the contours by Σ_{gas} and place them in 10 bins of equal size, or fewer if that leaves a cloud with < 20 contours per bin. (Recall that Σ_{gas} is the mean gas surface density inside a given contour, not the contour level itself, so two contours at the same level still generally have different Σ_{gas} .) Within each bin, we denote the 16th, 50th, and 84th percentiles of ϵ_{ff} (for both $\epsilon_{\text{ff},\text{sph}}$ and $\epsilon_{\text{ff},g}$) as $\epsilon_{\text{ff},16}$, $\epsilon_{\text{ff},50}$, and $\epsilon_{\text{ff},84}$. We plot these quantities as a function of Σ_{gas} in Fig. 6. We then define the mean star-formation efficiency for one cloud ($\langle \epsilon_{\text{ff}} \rangle$) as ¹

$$\langle \epsilon_{\text{ff}} \rangle = \frac{\int_{\log \Sigma_{\text{gas},\min}}^{\log \Sigma_{\text{gas},\max}} \epsilon_{\text{ff},50} d(\log \Sigma_{\text{gas}})}{\log \Sigma_{\text{gas},\max} - \log \Sigma_{\text{gas},\min}}, \quad (5)$$

where, $\Sigma_{\text{gas},\min}$ and $\Sigma_{\text{gas},\max}$ are the minimum and maximum contour surface density available for a given cloud; in terms of Fig. 6, $\langle \epsilon_{\text{ff}} \rangle$ is simply the mean value of the coloured line for each cloud. We evaluate this integral by approximating it as a finite sum over our groups. Similarly, we define the mean star-formation efficiency

¹In both equation (5) and (6), $\epsilon_{\text{ff},16}$, $\epsilon_{\text{ff},50}$, and $\epsilon_{\text{ff},84}$ are functions of Σ_{gas} .

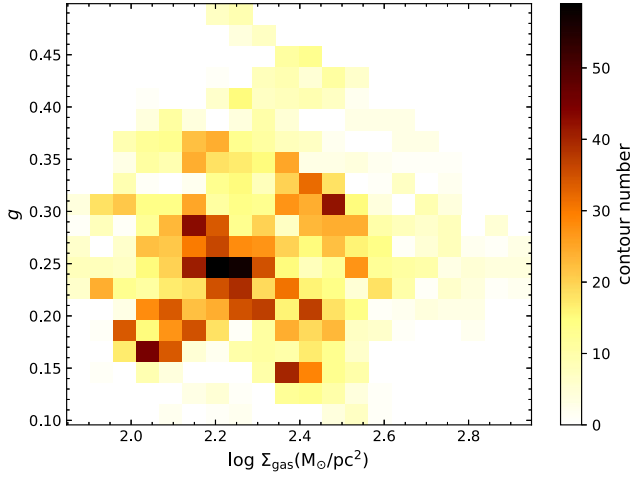


Figure 5. 2D histogram plot of g versus $\log(\Sigma_{\text{gas}})$. The values are determined from the unsmeared contours after all selections, and the colour shows the number of contours in the bin.

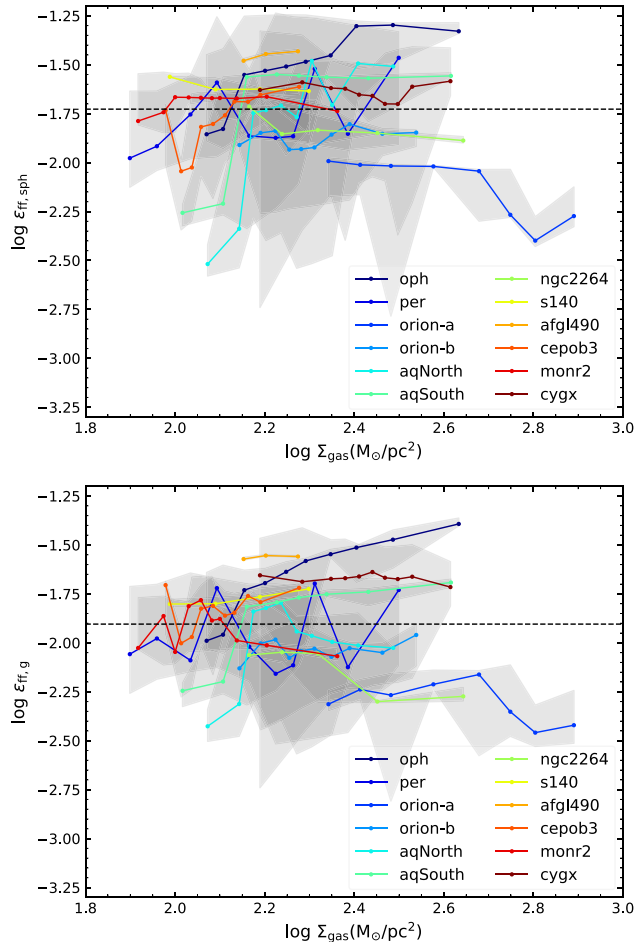


Figure 6. Distributions of $\log \epsilon_{\text{ff,sph}}$ (top panel) and $\log \epsilon_{\text{ff,g}}$ (bottom panel) as a function of $\log \Sigma_{\text{gas}}$. For each cloud, the coloured line and grey band show the 50th percentile and 16–84th percentile range of ϵ_{ff} in a bin of $\log \Sigma_{\text{gas}}$. The black dashed lines show the median values $\langle \epsilon_{\text{ff,sph}} \rangle$ and $\langle \epsilon_{\text{ff,g}} \rangle$ over all clouds.

Table 1. Estimates of $\langle \epsilon_{\text{ff}} \rangle$ and σ for individual clouds, using both the spherical assumption (values with subscript ‘sph’) and the Gini model equation (2) (values with subscript ‘g’); $\Delta\sigma = \sigma_{\text{sph}} - \sigma_g$. The column $\log \Sigma_{\text{gas}}$ reports the (min, max) contour average surface density measured for each cloud. Finally, the last three rows list the median, mean, and standard deviation (STD) values of the corresponding columns.

Cloud	$\log \langle \epsilon_{\text{ff,sph}} \rangle$	$\log \langle \epsilon_{\text{ff,g}} \rangle$	σ_{sph} (dex)	σ_g (dex)	$\Delta\sigma$ (dex)	$\log \Sigma_{\text{gas}}$ ($M_{\odot} \text{ pc}^{-2}$)
Ophiuchus	−1.45	−1.59	0.18	0.13	0.05	(2.05, 2.79)
Persus	−1.76	−1.97	0.28	0.31	−0.03	(1.85, 2.67)
Orion-A	−2.12	−2.29	0.13	0.15	−0.02	(2.24, 3.00)
Orion-B	−1.86	−2.03	0.19	0.16	0.03	(2.10, 2.64)
Aquila-N	−1.79	−2.03	0.31	0.23	0.08	(2.02, 2.56)
Aquila-S	−1.69	−1.84	0.18	0.11	0.07	(1.92, 2.78)
NGC 2264	−1.84	−2.18	0.04	0.05	−0.01	(1.97, 2.77)
S140	−1.62	−1.78	0.04	0.03	0.01	(1.95, 2.36)
AFGL 490	−1.45	−1.56	0.01	0.00	0.01	(2.14, 2.32)
Cep OB3	−1.76	−1.82	0.13	0.11	0.02	(1.92, 2.41)
Mon R2	−1.69	−1.97	0.06	0.09	−0.03	(1.77, 2.48)
Cygnus-X	−1.63	−1.67	0.41	0.40	0.01	(1.90, 2.78)
Median	−1.73	−1.90	0.16	0.12	0.01	–
Mean	−1.72	−1.89	0.16	0.15	0.02	–
STD	0.18	0.22	–	–	–	–

dispersion σ as

$$\sigma = \frac{\int_{\log \Sigma_{\text{gas,min}}}^{\log \Sigma_{\text{gas,max}}} (\log \epsilon_{\text{ff,84}} - \log \epsilon_{\text{ff,16}}) d(\log \Sigma_{\text{gas}})}{2(\log \Sigma_{\text{gas,max}} - \log \Sigma_{\text{gas,min}})}, \quad (6)$$

where, we again evaluate numerically as a finite sum over our bins of Σ_{gas} . In terms of Fig. 6, σ is simply half of the mean width of the grey band that surrounds each of the coloured lines.

We report the $\langle \epsilon_{\text{ff}} \rangle$ and σ values we measure using the spherical assumption (denoted by subscript sph) and with equation (2) (subscript g) for all 12 clouds in Table 1. After applying our model, the median value of $\log \langle \epsilon_{\text{ff}} \rangle$ decreases from $\log \langle \epsilon_{\text{ff,sph}} \rangle = -1.73$ to $\log \langle \epsilon_{\text{ff,g}} \rangle = -1.90$. This is consistent with the prediction in H21 that use of the spherical assumption leads to a ~ 0.13 dex overestimation of ϵ_{ff} . We also measure the difference in dispersion $\Delta\sigma = \sigma_{\text{sph}} - \sigma_g$ derived using the spherical assumption versus using equation (2) for each cloud. We find that eight of the 12 studied clouds yield positive $\Delta\sigma$, corresponding to a reduction in the dispersion; the mean reduction is $\Delta\sigma_{\text{mean}} = 0.02$ dex. This demonstrates that our model does decrease the dispersion, but less than the ~ 0.15 dex found when testing the method on simulated data in H21. This is likely due to the difference between the simulated data and observations. H21 calibrate their method based on simulations from Cunningham et al. (2018) that use periodic boundary conditions, so the column-density maps used in the calibration are from infinitely large self-similar clouds. The observed clouds, however, are from of finite size, so, for example, they can contain large-scale density gradients that are absent in periodic boxes. This suggests that we might obtain an improved version of equation (2) by analysing a zoom-in galactic simulation.

For all 12 clouds, we determine the STDs of both types of $\langle \epsilon_{\text{ff}} \rangle$ values: $\text{STD}_{\text{sph}} = 0.18$, and $\text{STD}_g = 0.22$. There is a slight increase after applying the H21 model, the reason for which might be that there are real physical differences between clouds that we have uncovered by not adopting the uniform spherical assumption. Given the relatively small $\Delta\sigma_{\text{median}}$ we obtain, it is also interesting to ask whether we could forgo individualized corrections altogether, and simply adopt the median value $g = 0.24$ for all contours. Doing

so would still produce a 0.1 dex median value decrease in ϵ_{ff} , while leaving the dispersion unchanged. However, such an approach would miss an important subtlety: while $g = 0.24$ is the median value for all contours on all scales, the value of g also changes systematically with size scale: on the largest scales of the 12 clouds we study, $g_{\text{median}} = 0.35$. Properly accounting for this is crucial to obtaining the correct changes in ϵ_{ff} versus Σ_{gas} , and thus the correct $\Delta\sigma$ values within individual clouds. For this reason, we prefer to use individual-contour corrections when possible.

5 CONCLUSIONS

We use a new method proposed by H21 to combine column-density maps derived from *Herschel* with YSOs from the SESNA catalogue to determine the star-formation efficiency per free-fall time ϵ_{ff} in 12 nearby clouds. Our method provides a more realistic estimate of the mean volume densities of clouds seen in projection, reducing the error incurred by assuming that projected clouds are spherical, and allowing higher precision estimates of ϵ_{ff} than previously possible. We find that the spherical assumption leads to ~ 0.1 dex overestimation of $\log(\epsilon_{\text{ff}})$, and also increases the estimated intracloud dispersion in $\log(\epsilon_{\text{ff}})$ by ~ 0.02 dex on average. With our new method, we find that our sample of 12 clouds has a median star-formation efficiency per free-fall time $\log(\epsilon_{\text{ff}}) = -1.9$, and the median spread in $\log(\epsilon_{\text{ff}}) = 0.12$ dex within a single cloud. The intercloud dispersion in $\log(\epsilon_{\text{ff}})$ is nearly identical, at 0.2 dex, and this value is, within the uncertainties, unaffected by the use of the H21 model for the gas density. This strongly suggests that the intracloud dispersion we are measuring reflects a real variation in cloud properties, not an observational error.

Our results confirm the existence of a universal $\epsilon_{\text{ff}} \sim 0.01$ value, and, importantly, let us identify a real ≈ 0.2 dex spread from cloud to cloud with 3D cloud geometry considered for the first time. As discussed in Pokhrel et al. (2021), such a small spread is in tension with models where star formation is regulated mainly by galactic-scale processes, but individual molecular clouds undergo rapid collapse (e.g. Kim et al. 2011; Ostriker & Shetty 2011; Faucher-Giguère et al. 2013). These models predict a much larger dispersion. Conversely, however, our measured spread in ϵ_{ff} can be used to evaluate the spread in parameters that enter models for cloud-scale regulation of star formation, which do predict dispersions comparable in size to the observed one. For example, in the turbulence-regulated star formation of Krumholz & McKee (2005), a ~ 0.2 dex spread in ϵ_{ff} could naturally be explained by a $\sigma_{\alpha} \sim 0.3$ dex spread in cloud virial parameters (or a $\sigma_{\mathcal{M}} \sim 0.7$ dex spread in Mach number), while in the similar model of Hennebelle & Chabrier (2011) the required dispersion is $\sigma_{\alpha} \sim 0.8$ dex ($\sigma_{\mathcal{M}} \sim 0.6$ dex), and for the model of Padoan et al. (2012) would require $\sigma_{\alpha} \sim 0.5$ dex. For comparison, Lee et al. (2016) study 195 star-forming giant molecular clouds and find a scatter of 0.32 dex in the virial parameter. Thus, observed clouds have approximately the level of dispersion in virial parameter required to reproduce the spread we see in ϵ_{ff} . In future work, we can use the same technique of high-precision estimates of ϵ_{ff} deployed here to search not just for the dispersion in ϵ_{ff} , but to look for systematic variations with virial parameter or other cloud properties, thereby opening up a new method for testing theories of star formation.

ACKNOWLEDGEMENTS

We acknowledge the anonymous referee for the insightful advice on this manuscript. M. R. K. acknowledges funding from Australian Research Council awards DP190101258 and FT180100375. R. P.

and R. A. G. acknowledge support from National Aeronautics and Space Administration (NASA) Astrophysics Data Analysis Program (ADAP) awards NNX15AF05G, 80NSSC18K1564, and NNX17AF24G. R. P. acknowledges funding from NASA ADAP award 80NSSC18K1564, and R. A. G. acknowledges funding from NASA ADAP awards NNX11AD14G and NNX13AF08G. We further acknowledge high-performance computing resources provided by the Australian National Computational Infrastructure (grants jh2 and ek9) through the National and Australian National University (ANU) Computational Merit Allocation Schemes, and by the Leibniz Rechenzentrum and the Gauss Centre for Supercomputing (grant pr32lo).

This research has made use of data from the Herschel Gould Belt survey (HGBS) project, a Herschel Key Programme jointly carried out by SPIRE Specialist Astronomy Group 3 (SAG 3), scientists of several institutes in the PACS Consortium (CEA Saclay, INAF-IFSI Rome, and INAF-Arcetri, KU Leuven, MPIA Heidelberg), and scientists of the Herschel Science Center (HSC).

DATA AVAILABILITY

The data underlying this article will be shared upon reasonable request to the corresponding author.

REFERENCES

- André P. et al., 2010, *A&A*, 518, L102
 André P., Di Francesco J., Ward-Thompson D., Inutsuka S.-I., Pudritz R. E., Pineda J., 2014, in Beuther H., Klessen R. S., Dullemond C. P., Henning T., eds, *Protostars and Planets VI*, Univ. Arizona Press, Tucson
 Arzoumanian D. et al., 2011, *A&A*, 529, L6
 Chabrier G., 2003, *PASP*, 115, 763
 Cunningham A. J., Krumholz M. R., McKee C. F., Klein R. I., 2018, *MNRAS*, 476, 771
 Dobashi K., Uehara H., Kandori R., Sakurai T., Kaiden M., Umemoto T., Sato F., 2005, *PASJ*, 57, S1
 Dunham M. M. et al., 2014, in Beuther H., Klessen R. S., Dullemond C. P., Henning T., eds, *Protostars and Planets VI*. Univ. Arizona Press, Tucson, p. 195
 Dunham M. M. et al., 2015, *ApJS*, 220, 11
 Elmegreen B. G., Parravano A., 1994, *ApJ*, 435, L121
 Evans N. J. et al., 2009, *ApJS*, 181, 321
 Evans N. J., Heiderman A., Vutisalchavakul N., 2014, *ApJ*, 782, 114
 Faucher-Giguère C.-A., Quataert E., Hopkins P. F., 2013, *MNRAS*, 433, 1970
 Federrath C., 2013, *MNRAS*, 436, 3167
 Federrath C., Klessen R. S., 2012, *ApJ*, 761, 156
 Froebrich D., Rowles J., 2010, *MNRAS*, 406, 1350
 Goodman A. A., Pineda J. E., Schnee S. L., 2009, *ApJ*, 692, 91
 Gutermuth R. A. et al., 2008, *ApJ*, 674, 336
 Gutermuth R. A., Megeath S. T., Myers P. C., Allen L. E., Pipher J. L., Fazio G. G., 2009, *ApJS*, 184, 18
 Hennebelle P., Chabrier G., 2011, *ApJ*, 743, L29
 Heyer M., Gutermuth R., Urquhart J. S., Csengeri T., Wienen M., Leurini S., Menten K., Wyrowski F., 2016, *A&A*, 588, A29
 Hu Z., Krumholz M. R., Federrath C., Pokhrel R., Gutermuth R. A., 2021, *MNRAS*, 502, 5997
 Kainulainen J., Beuther H., Henning T., Plume R., 2009, *A&A*, 508, L35
 Kainulainen J., Hacar A., Alves J., Beuther H., Bouy H., Tafalla M., 2016, *A&A*, 586, A27
 Kim C.-G., Kim W.-T., Ostriker E. C., 2011, *ApJ*, 743, 25
 Krumholz M. R., McKee C. F., 2005, *ApJ*, 630, 250
 Krumholz M. R., McKee C. F., 2020, *MNRAS*, 494, 624
 Krumholz M. R., Tan J. C., 2007, *ApJ*, 654, 304–315
 Krumholz M. R., Leroy A. K., McKee C. F., 2011a, *ApJ*, 731, 25
 Krumholz M. R., Dekel A., McKee C. F., 2011b, *ApJ*, 745, 69

- Krumholz M. R., Dekel A., McKee C. F., 2012, *ApJ*, 745, 69
- Krumholz M. R., McKee C. F., Bland-Hawthorn J., 2019, *ARA&A*, 57, 227
- Kryukova E. et al., 2014, *AJ*, 148, 11
- Kryukova E., Megeath S. T., Gutermuth R. A., Pipher J., Allen T. S., Allen L. E., Myers P. C., Muzerolle J., 2012, *AJ*, 144, 31
- Lada C. J., Lombardi M., Roman-Zuniga C., Forbrich J., Alves J. F., 2013, *ApJ*, 778, 133
- Lawrence A. et al., 2007, *MNRAS*, 379, 1599
- Lee E. J., Miville-Deschênes M.-A., Murray N. W., 2016, *ApJ*, 833, 229
- Lombardi M., Alves J., Lada C. J., 2010, *A&A*, 519, L7
- Lucas P. W. et al., 2008, *MNRAS*, 391, 136
- Nieva M.-F., Przybilla N., 2012, *A&A*, 539, A143
- Ochsendorf B. B., Meixner M., Roman-Duval J., Rahman M., Evans N. J., 2017, *ApJ*, 841, 109
- Ostriker E. C., Shetty R., 2011, *ApJ*, 731, 41
- Padoan P., Haugbølle T., Nordlund Å., 2012, *ApJ*, 759, L27
- Pokhrel R. et al., 2016, *MNRAS*, 461, 22
- Pokhrel R. et al., 2020, *ApJ*, 896, 60
- Pokhrel R. et al., 2021, *ApJ*, 912, L19
- Salim D. M., Federrath C., Kewley L. J., 2015, *ApJ*, 806, L36
- Schneider N. et al., 2011, *A&A*, 529, A1
- Schneider N. et al., 2015, *A&A*, 575, A79
- Schneider S., Elmegreen B. G., 1979, *ApJS*, 41, 87
- Skrutskie M. F. et al., 2006, *AJ*, 131, 1163
- Utomo D. et al., 2018, *ApJ*, 861, L18
- Zuckerman B., Evans N. J., 1974, *ApJ*, 192, L149

This paper has been typeset from a $\text{\TeX}/\text{\LaTeX}$ file prepared by the author.